Theoretical prediction of superconductivity in two-dimensional hydrogenated metal diboride: M_2B_2H (M = Al, Mg, Mo, W)

Yu-Lin Han,[1] Hao-Dong Liu,[1] Na Jiao,[1] Meng-Meng Zheng,[1] Hong-Yan Lu,[1,*] Bao-Tian Wang,[2,3,†] and Ping Zhang[1,4,‡]
[1]*School of Physics and Physical Engineering, Qufu Normal University, Qufu 273165, China*
[2]*Institute of High Energy Physics, Chinese Academy of Sciences, Beijing 100049, China*
[3]*Spallation Neutron Source Science Center, Dongguan 523803, China*
[4]*Institute of Applied Physics and Computational Mathematics, Beijing 100088, China*

(Received 25 July 2023; accepted 16 October 2023; published 3 November 2023)

In recent years, superconductivity in two-dimensional (2D) layered metal borides has aroused much interest. Here, based on first-principles calculations, we theoretically report four 2D hydrogenated metal diborides: M_2B_2H ($M = $ Al, Mg, Mo, W), and investigate their geometrical structures, electronic structures, phonon dispersions, thermal stability, dynamic stability, electron-phonon coupling (EPC), superconducting properties, and so on. Results reveal that the introduction of hydrogen atoms expands the frequency range of the phonon spectrum of monolayer M_2B_2, and significantly increases the EPC. We systematically analyze the specific origins of superconductivity in these hydrogenated low-dimensional systems. The obtained EPC constants λ of M_2B_2H ($M = $ Al, Mg, Mo, W) are 2.93, 0.86, 1.09, and 1.40, and the corresponding superconducting transition temperatures (T_c) are 52.6, 23.2, 21.5, and 18.6 K, respectively. By further applying electron/hole doping or biaxial tensile strain, the T_c can be further increased, with the highest T_c of 60.2 K in Al_2B_2H under 0.4% biaxial tensile strain. The predicted M_2B_2H provides a new platform for 2D superconductivity and may have potential applications in 2D nanodevices.

DOI: 10.1103/PhysRevMaterials.7.114802

I. INTRODUCTION

With the rapid progress of low-dimensional nanotechnology, the fabrication of various types of two-dimensional (2D) materials becomes possible, such as graphene [1], silicene [2,3], transition-metal dichalcogenides [4–7], *h*-BN [8,9], etc., which have drawn much attention in condensed-matter physics and materials science. Two-dimensional superconductors are continuously drawing much interest due to their potential technology applications [10], such as the realization of next-generation quantum information techniques. Exploring 2D superconductors with high T_c has become a hot spot in condensed matter physics [11]. Actually, it has been theoretically predicted that alkali metal Li and Ca deposited graphenes, i.e., LiC_6 and CaC_6, can be superconductors with T_c of 8.1 and 1.4 K, respectively [12]. Later, angle-resolved photoemission spectroscopy (ARPES) proof for a superconducting gap in LiC_6 with an estimated T_c about 5.9 K was experimentally reported by Ludbrook *et al.* [13]. The aluminum-deposited graphene AlC_8 was also theoretically predicted to be a superconductor with T_c of 22.2 K through hole doping and biaxial tensile straining [14]. Additionally, Savini *et al.* theoretically investigated that carrier doping and tensile strain can also induce conventional superconductivity in graphene [15]. Similar calculations were also carried out for silicene and phosphorene, with T_c found to be about 15.5 and 12.2 K, respectively, for electron-doped silicene and phosphorene under the application of tensile strain [16–18].

According to the Bardeen-Cooper-Schrieffer (BCS) theory, elements with light mass, due to their relatively high Debye temperature, are able to generate strong phonon-mediated superconducting pairing. Ashcroft predicted that dense metallic hydrogen may be a candidate for high-temperature superconductivity in 1968 [19]. However, the superhigh pressure required to fabricate dense metallic hydrogen exceeds 400 GPa and high-temperature superconductivity in pure hydrogen systems still needs further experimental confirmation [20,21].

As the lightest nonmetallic element besides hydrogen and helium, boron or its compounds have been extensively studied. Borophene, a 2D boron sheet possessing various novel physical properties [22–25], is expected to serve as a new functional material or a precursor for constructing boron nanotubes [26] and has been successfully grown on the Ag (111) surface through directly evaporating a pure boron source. Two types of borophene structures were unveiled in experiments, namely β_{12} and χ_3 borophene [27,28]. Subsequent theoretical calculations predicted them to be superconductors with T_c to be 18.7 and 24.7 K, respectively [25]. Bilayer borophenes, i.e., BL-B_6 and BL-B_{30}, were also predicted to be superconductors with T_c of 11.9 and 4.9 K, respectively [29].

Moreover, except for pure boron systems, a series of 2D metal borides have been systematically investigated, including orthorhombic and hexagonal MB_6, which were theoretically predicted to be superconductors with T_c in the range of

---

[*] hylu@qfnu.edu.cn
[†] wangbt@ihep.ac.cn
[‡] zhang_ping@iapcm.ac.cn

1.4–22.6 K [30]. Metal borides MB_4, where M represent Li, Be, Mg, Al, Ca, Ga, have been predicted to be superconductors with T_c exceeding 20 K [31–33]. h-MnB_3, contains two boron kagome layers sandwiched with Mn atoms, exhibits metallic properties with T_c of 24.9 K. In addition, evidence of three-gap nature with high T_c of 41.5 and 53.0 K were found through theoretical calculations in InB_2 and InB_4 monolayer films, respectively [34]. Surface superconductivity with high T_c up to ~90 K was predicted at the surfaces of ternary compound $CaB_{n+1}C_{n+1}$ ($n = 1, 2, 3, \ldots$) films [35].

Previous works have indicated that hydrogenation can modify the electronic and magnetic properties of 2D systems and may also produce high-T_c superconducting states. For instance, fully hydrogenated graphene, frequently referred to as graphane, with hydrogen atoms bonded to carbon atoms alternatively on both sides of the carbon plane, was theoretically predicted to be a phonon-mediated superconductor with T_c up to 90 K under hole doping [36]. Similarly, it was predicted that, after hydrogenating the P atoms, monolayer PC_3 turns from a semiconductor into a superconducting phase with T_c being ~31.0 K [37]. Fully hydrogenated monolayer hexagonal boron nitride H_2BN, which has a direct band gap, can be converted into a superconductor with T_c over 80 K under hole doping and biaxial tensile strain [38]. Most recently, Liu *et al.* found through theoretical calculations that the previously synthesized Janus MoSH monolayer, obtained by substituting the top layer S of MoS_2 with H atoms [39], is a two-gap superconductor with T_c being about 28.5 K, which can be boosted to 37.3 K via electron doping [40]. Additionally, it was predicted that hydrogenated CaB_3, i.e., $HCaB_3$, with a boron kagome lattice, is a superconductor with T_c close to the McMillan limit (39 K) [41]. Previous calculations demonstrated a three-gap nature with T_c of 20 K in the monolayer MgB_2 [42], while the hydrogenated MgB_2 yields a high T_c of 67 K, which can be further boosted to over 100 K by merely 5% of biaxial tensile strain [43]. Our recent study shows that hydrogenated titanium diboride $Ti_2B_2H_4$, converts the Ti_2B_2 from a normal metal into a superconductor with T_c of 48.6 K, which can be further boosted to 69.4 K by applying biaxial compressive strain [44].

Therefore, it is of great significance to study the effects of hydrogenation on the electronic properties and possible high-temperature superconductivities in 2D borides. In the present work, we report four 2D hydrogenated metal diborides: M_2B_2H (M = Al, Mg, Mo, W), with one honeycomb boron atomic layer sandwiched by two layers of metal atoms, while H atoms are located above the boron atoms and bond only with metal atoms. We systematically investigate their crystal structures, bonding properties, electronic properties, phonon dispersions, electron-phonon coupling (EPC) strength, and possible superconductivity by performing first-principles calculations. Based on the Eliashberg function, by analytically solving the McMillan-Allen-Dynes formula, we find that these 2D hydrogenated metal diborides are all phonon-mediated superconductors, with the EPC constants λ of 2.93, 0.86, 1.09, and 1.40, and the corresponding T_cs of 52.6, 23.2, 21.5, and 18.6 K, respectively. The underlying mechanism of their superconductivity is carefully analyzed. In addition, since the external regulatory measures play a critical role in regulating the electronic structure and superconductivity of the 2D systems, the effect of electron/hole doping and tensile/compressive strain engineering on EPC strength and superconducting properties of M_2B_2H monolayers are also systematically discussed.

II. COMPUTATIONAL DETAILS

First-principles calculations within the framework of density functional theory (DFT) [45] are performed by using the well-established Quantum-ESPRESSO (QE) package [46,47]. The Perdew-Burke-Ernzerhof (PBE) parametrized generalized gradient approximation (GGA) is chosen to describe the exchange-correlation energy [48,49]. The projector-augmented-wave (PAW) pseudopotential [50] is utilized to model the interaction between electrons and ionic cores with plane-wave kinetic-energy cutoff and energy cutoff for charge density of 80 and 800 Ry, respectively. Lattice constants and atomic positions are fully optimized by using the conjugated gradient algorithm and the energy and force convergence criteria are set to be 10^{-8} and 10^{-7} Ry a.u.$^{-1}$, respectively. To decouple the adjacent layers, a sufficiently vacuum space of 25 Å along the z direction is adopted. Density functional perturbation theory (DFPT) [51] is employed to calculate the dynamics matrix and EPC parameter within the range of linear response and as input to solve the isotropic Eliashberg equation. The phonon and EPC properties are calculated on a $12 \times 12 \times 1$ q-point grid, and a denser $48 \times 48 \times 1$ k-point grid is used for evaluating an accurate electron-phonon interaction matrix. The *ab initio* molecular dynamics (AIMD) simulations implemented in the Vienna *Ab initio* Simulation Package (VASP) [52] are employed at 400 K to investigate the thermal stability of these 2D M_2B_2H monolayers. $3 \times 3 \times 1$ supercells with a time step of 1.5 fs and total simulation of 6 ps are adopted.

The EPC properties and possible superconductivity are calculated based on the Eliashberg equations. The total EPC constant λ is obtained via isotropic Eliashberg function [53–55]

$$\alpha^2F(\omega) = \frac{1}{2\pi N(E_F)} \sum_{\mathbf{q}\nu} \delta(\omega - \omega_{\mathbf{q}\nu}) \frac{\gamma_{\mathbf{q}\nu}}{\omega_{\mathbf{q}\nu}}, \tag{1}$$

$$\lambda = 2\int_0^\infty \frac{\alpha^2F(\omega)}{\omega}\, d\omega = \sum_{\mathbf{q}\nu} \lambda_{\mathbf{q}\nu}, \tag{2}$$

where $\alpha^2F(\omega)$ is the Eliashberg function, $N(E_F)$ is the electronic DOS at the Fermi level, $\omega_{\mathbf{q}\nu}$ is the phonon frequency of the νth phonon mode with wave vector $\mathbf{q}$, and $\gamma_{\mathbf{q}\nu}$ is the phonon linewidth. The $\gamma_{\mathbf{q}\nu}$ can be estimated by

$$\gamma_{\mathbf{q}\nu} = \frac{2\pi\omega_{\mathbf{q}\nu}}{\Omega_{BZ}} \sum_{\mathbf{k},n,m} \left|g^{\nu}_{\mathbf{k}n,\mathbf{k}+\mathbf{q}m}\right|^2 \delta(\epsilon_{\mathbf{k}n} - E_F) \times \delta(\epsilon_{\mathbf{k}+\mathbf{q}m} - E_F), \tag{3}$$

where Ω_{BZ} is the volume of the Brillouin zone (BZ), $\epsilon_{\mathbf{k}n}$ and $\epsilon_{\mathbf{k}+\mathbf{q}m}$ indicate the Kohn-Sham energy, and $g^{\nu}_{\mathbf{k}n,\mathbf{k}+\mathbf{q}m}$ represents the screened electron-phonon matrix element. $\lambda_{\mathbf{q}\nu}$ is the EPC constant for phonon mode $\mathbf{q}\nu$, which is defined as

$$\lambda_{\mathbf{q}\nu} = \frac{\gamma_{\mathbf{q}\nu}}{\pi\hbar N(E_F)\omega^2_{\mathbf{q}\nu}}. \tag{4}$$

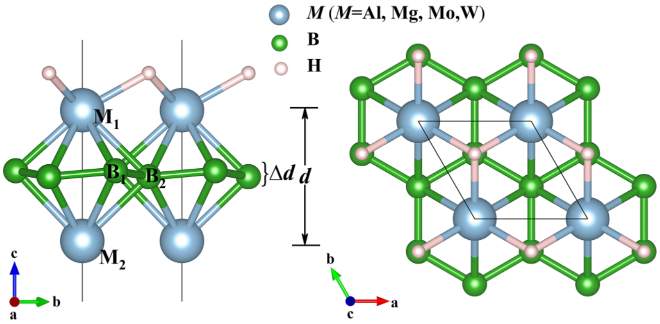

FIG. 1. Side and top views of the M_2B_2H (M = Al, Mg, Mo, W) monolayers. The metal, boron, and hydrogen atoms are represented by blue, green, and pink spheres, respectively. The unit cell is shown by the black solid line.

T_c is estimated by the modified McMillan formula [55]

$$T_c = \frac{\omega_{\log}}{1.2} \exp\left[\frac{-1.04(1+\lambda)}{\lambda - \mu^*(1+0.62\lambda)}\right]. \tag{5}$$

The hysteretic Coulomb pseudopotential μ^* in Eq. (5) is set to 0.1, and the logarithmic average of the phonon frequencies $\omega_{\log}$ is defined as

$$\omega_{\log} = \exp\left[\frac{2}{\lambda}\int_0^{\omega} \alpha^2F(\omega)\frac{\ln\omega}{\omega}d\omega\right]. \tag{6}$$

For the EPC cases $\lambda > 1.30$, T_c is estimated by the full Allen-Dynes formula [55]

$$T_c = f_1 f_2 \frac{\omega_{\log}}{1.2} \exp\left[\frac{-1.04(1+\lambda)}{\lambda - \mu^*(1+0.62\lambda)}\right]. \tag{7}$$

Here, f_1 and f_2 are the strong-coupling correction factor and the shape correction factor, respectively, with

$$f_1 = \left\{1 + \left[\frac{\lambda}{2.46(1+3.8\mu^*)}\right]^{3/2}\right\}^{1/3}, \tag{8}$$

$$f_2 = 1 + \frac{[(\omega_2/\omega_{\log}) - 1]\lambda^2}{\lambda^2 + 3.312(1+6.3\mu^*)^2(\omega_2/\omega_{\log})^2}, \tag{9}$$

in which ω_2 is defined as

$$\omega_2 = \left[\frac{2}{\lambda}\int_0^{\omega_{max}} \alpha^2F(\omega)\omega d\omega\right]^{1/2}. \tag{10}$$

III. RESULTS AND DISCUSSION

A. Lattice structure

The optimized lattice structures of monolayer M_2B_2H (M = Al, Mg, Mo, W) possess trigonal symmetry with space group of $P3/m1$ (No. 156). Their lattice structures in the side and top views are shown in Fig. 1. The honeycomb boron atomic layer is sandwiched by two layers of metal atoms standing above/below the centers of the honeycombs. The H atoms are located above the boron atoms and bond only with the metal atoms. For metal and B atomic layers in monolayer M_2B_2, upper and lower metal atoms bond with six B atoms to form a dodecahedron with the triple layers stacking in *ABA* order. Meanwhile, the B atoms are anchored and stabilized by the two metal layers, leading to the high stability of these 2D materials. The detailed optimized lattice parameters are listed in Table I. The lattice constants a of monolayer Al_2B_2H, Mg_2B_2H, Mo_2B_2H, and W_2B_2H are 2.962, 3.072, 3.043, and 2.985 Å, respectively. It is found that the introduction of H atom makes the honeycomb boron layer no longer flat but wrinkled to different degrees. This fold strength gradually decreases from Al and Mg to Mo and W structures, especially in Al_2B_2H, but becomes almost no longer perceptible in Mo_2B_2H and W_2B_2H. For comparison, the optimized lattice parameters of M_2B_2 (M = Al, Mg, Mo, W) are also listed in Table I, which is quite consistent with previous work [33]. Hydrogenation slightly increases the lattice constant a of Al_2B_2, and on the contrary, slightly decreases those of Mg_2B_2, Mo_2B_2, and W_2B_2.

To analyze the bonding properties, we have performed the Bader charge analysis [56], electron localization function (ELF) [57], and line charge distribution at the corresponding bond point (CD_b) [58] along the nearest B-B, M-B, and M-H bonds. Pseudopotentials with valence electrons containing $3s^23p^1$ for Al atoms, $3s^23p^0$ for Mg atoms, $4d^55s^1$ for Mo atoms, $5d^46s^2$ for W atoms, $2s^22p^1$ for B atoms, and $1s^1$ for H atoms are adopted. By analyzing the ionicity according to the Bader charge, displayed in Table II, it can be found that Al atoms transfer the most electrons, reaching 3.031e, while the least Mo atoms transferred 1.246e. The metal atoms always lose electrons, and the lost electrons transfer to their neighboring H atoms and graphene-like boron atomic layer, so as to strengthen the bonding of B-B. The CD_b(B-B) values for these four M_2B_2H monolayers vary in the range of 0.119–0.133 e per a.u.^{3}, which are higher than that of the Si covalent bond (0.104 e per a.u.^{3}) [58], indicating that the B

TABLE I. Lattice parameter a, perpendicular distance between metal atomic layer d (Å), atomic fluctuation height of boron atomic layer Δd (Å), bond lengths (Å), and cohesive energy (eV/atom) of M_2B_2 and M_2B_2H monolayers.

	a	d	Δd	M_1-B_1/M_2-B_1	M_1-B_2/M_2-B_2	B_1-B_2	M_1-H	E_{coh}
Al_2B_2	2.937	3.471		2.427	2.427	1.696		4.97
Mg_2B_2	3.105	3.430		2.476	2.476	1.786		3.96
Mo_2B_2	3.067	2.847		2.272	2.272	1.771		8.29
W_2B_2	3.045	2.882		2.273	2.273	1.758		8.46
Al_2B_2H	2.962	3.364	0.153	2.315/2.486	2.421/2.377	1.717	1.957	4.64
Mg_2B_2H	3.072	3.498	0.036	2.522/2.460	2.547/2.436	1.774	2.022	3.91
Mo_2B_2H	3.043	2.937	0.004	2.316/2.264	2.315/2.265	1.757	2.053	7.44
W_2B_2H	2.985	3.085	0.005	2.337/2.289	2.334/2.293	1.723	2.038	7.55

TABLE II. Bader charge (Q_B) and charge density at the corresponding bond point (CD_b) for the 2D M_2B_2H.

	Q_{M_1}	Q_{M_2}	Q_{B_1}	Q_{B_2}	Q_H	CD_b M_1-B_1	CD_b M_1-B_2	CD_b M_2-B_1	CD_b M_2-B_2	CD_b B_1-B_1	CD_b M_1-H
Al_2B_2H	1.035	1.934	4.075	4.118	1.838	0.056	0.052	0.042	0.047	0.132	0.044
Mg_2B_2H	0.417	0.789	3.904	4.076	1.814	0.037	0.036	0.041	0.043	0.124	0.038
Mo_2B_2H	5.182	5.554	3.558	3.298	1.408	0.066	0.067	0.073	0.071	0.115	0.049
W_2B_2H	5.110	5.492	3.612	3.373	1.410	0.069	0.070	0.073	0.072	0.119	0.053

layers own slightly stronger covalent bonds than Si. The ELF values, as presented in Fig. S4 of the Supplemental Material (SM) [59], are about 0.8–0.9 between neighboring B atoms for these M_2B_2H monolayers, also suggesting the strong covalent bonds of the B layers. The B-B covalence has also been proved in previous works [30,60,61]. Additionally, charge transfer and small ELF values between M-B and M-H also suggest the formation of ionic bonds. Therefore, for the investigated 2D M_2B_2H, covalent bonding generally exists in B-B bonds, while ionic bonding exists between metals and nonmetals.

B. Stability

To explore the stability of these M_2B_2H monolayers, we calculate the phonon dispersions along the high-symmetry lines as well as the phonon density of states (PhDOS) to evaluate the dynamic stability. No imaginary modes confirms the lattice dynamic stability of these thin films. A detailed discussion of the phonon dispersions will be supplied later. In addition, thermal stability is essential for the practical application of these 2D M_2B_2H in nanoelectronic devices or electrode films. In order to investigate the thermal stability, AIMD simulations are performed with total simulation time of 6 ps at 400 K. Presented in Fig. S5 of the SM [59] are the variations of total energies with time for the M_2B_2H monolayers. The snapshots after 6 ps are also shown. It can be seen that their energy fluctuates around −208, −174, −338, and −367 eV, respectively, and the structures still maintain the integrity, proving their thermodynamical stability. Additionally, cohesive energy is a widely accepted parameter used to evaluate the stability of materials. The cohesive energy is calculated based on the following equations:

$$E_{\mathrm{coh}} = \frac{2E_M + 2E_{\mathrm{B}} - E_{M_2B_2}}{4} \tag{11}$$

for M_2B_2 and

$$E_{\mathrm{coh}} = \frac{2E_M + 2E_{\mathrm{B}} + E_{\mathrm{H}} - E_{M_2B_2H}}{5} \tag{12}$$

for M_2B_2H, where E_M, E_{B}, and E_{H} represent the total energies of the isolated metal, B, and H atoms, respectively; $E_{M_2B_2}$ and $E_{M_2B_2H}$ are the total energies of the 2D M_2B_2 and M_2B_2H. In view of this definition, materials with more positive E_{coh} indicate a higher chemical stability. The calculated cohesive energies of M_2B_2H are 4.64, 3.91, 7.44, and 7.55 eV/atom, respectively. The cohesive energies of these 2D M_2B_2H are larger than those of the previously computationally predicted and later experimentally fabricated 2D materials, such as phosphorene (3.61 eV/atom), silicene (3.71 eV/atom) [62], and Cu_2Si (3.46 eV/atom) [63,64]. This ensures the thermodynamic feasibility of these thin films and indicates that the predicted M_2B_2H monolayers are possible to be synthesized under appropriate experimental conditions.

C. Electronic structure

To investigate the electronic structure properties of monolayer M_2B_2H, the orbital-resolved band structure, electronic density of states (DOS), as well as the orbital-projected DOS (PDOS) are calculated and presented in Fig. 2. The corresponding Fermi surfaces (FSs) with high-symmetry path along Γ-M-K-Γ are shown in Fig. 3. The electronic structure properties of M_2B_2 monolayers are presented in Fig. S2 of the SM [59], with results quite consistent with previous research [33]. From the orbital-resolved band structures, it can be seen that all these 2D materials exhibit metallic properties, with several bands crossing the Fermi level. For Al_2B_2H, Mo_2B_2H, and W_2B_2H, metal atoms dominate the bands around the Fermi level and play a prominent role in their metallic properties, while B atomic orbitals have limited contribution, especially in Mo_2B_2H and W_2B_2H, in which B atoms have almost no component around the Fermi level. Things go a little differently for Mg_2B_2H, where B's contribution dominates. However, the role of Mg in it also cannot be ignored. More specifically, in Al_2B_2H, the projected orbitals that mainly dominate the E_F are Al $3s$ followed by B $2p_z$. Differently, for Mg_2B_2H, B atomic orbitals play a more prominent role than Mg, and the E_F is dominated by B $2p_z$, followed by Mg $3s$, while for Mo_2B_2H, $4d_{z^2}$ and $4d_{zx}/d_{yz}$ orbitals of Mo contribute almost equally to the Fermi level. For W_2B_2H, E_F is dominated by $5d_{z^2}$ and $5d_{zx}/d_{yz}$. The contribution of H atoms in these four structures to the composition of bands around the Fermi level is extremely limited. This is different from hydrogenated MgB_2, where the π-Hs state formed by hybridizing B-p_z and H-s orbitals carries the most DOS [43]. The above conclusions can also be confirmed from DOS and PDOS presented at the right of each band structure. The properties of energy bands crossing the Fermi level are also different. The conduction band crosses the Fermi level in Al_2B_2H, while for the remaining three cases it is the valence band.

Combining FSs, with the color drawn to indicate the relative Fermi velocity v_F, reflecting the different slopes of the bands that constitute the FS, and orbital-resolved band structure, it can be seen that for Al_2B_2H, only a single band is crossing the E_F, forming a large hexagonal Γ-centered hole pocket and two K-centered pockets, with an inner horseshoed electron pocket and external hole pocket. The highest v_F mainly originates from the band crossing the Fermi level along the Γ-M direction, while the low velocity mainly appears when crossing the hole pocket along the M-K directions. For Mg_2B_2H, three bands are crossing the Fermi level four times along the Γ-M and K-Γ directions, forming four Γ-centered pockets. The inner two are hole pockets, originating mainly from B $2p_x/p_y$, carrying the maximum and minimum

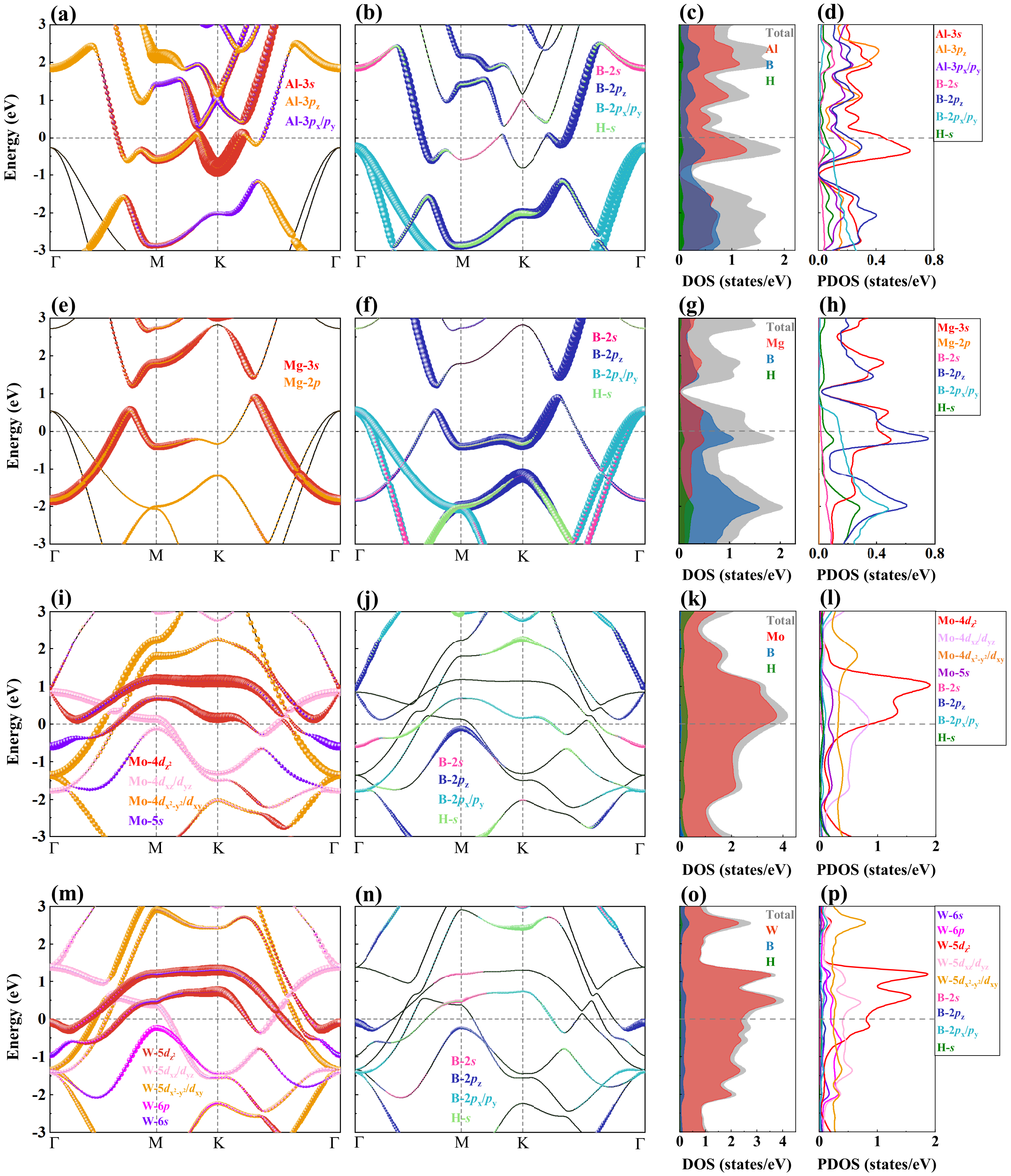

FIG. 2. Orbital-projected electronic band structures of (a), (b) Al_2B_2H; (e), (f) Mg_2B_2H; (i), (j) Mo_2B_2H; and (m), (n) W_2B_2H along high-symmetry line Γ-M-K-Γ. (c), (g), (k), (o): The total DOS and PDOS of M_2B_2H (M = Al, Mg, Mo, W). (d), (h), (l), (p): The PDOS for the specific orbitals of M_2B_2H. The Fermi level indicated by the dotted line is set to 0 eV.

v_F when crossing the E_F along the Γ-M directions, respectively. The two outer pockets are both mainly from the Mg 3s and B $2p_z$, with the inner one an electron pocket and the outer hexagonal-like hole pocket. For Mo_2B_2H, there are three, one, and two bands crossing the Fermi level along the Γ-M, M-K, and K-Γ directions, respectively. Centered around Γ is an electron pocket originating mainly from Mo $4d_{x^2-y^2}$, while M-centered is a horseshoed hole pocket dominated by Mo

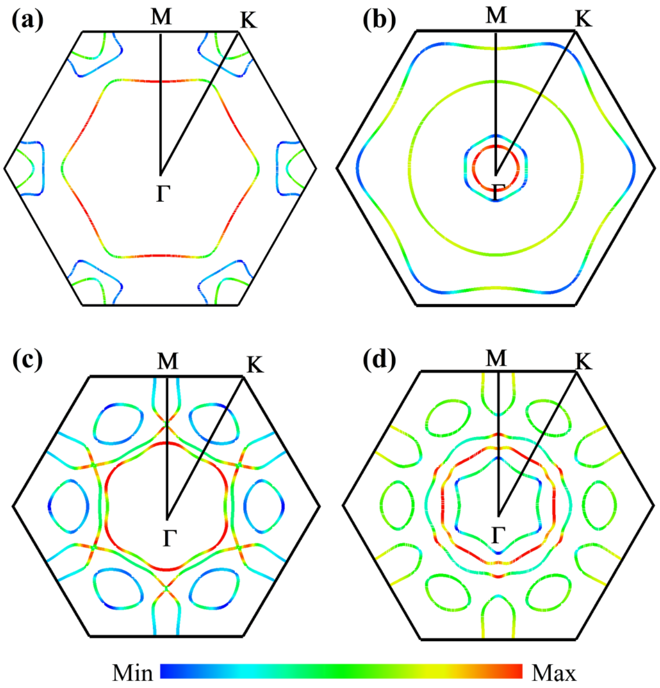

FIG. 3. FSs of (a) Al_2B_2H, (b) Mg_2B_2H, (c) Mo_2B_2H, and (d) W_2B_2H with the color drawn proportional to the magnitude of the Fermi velocity v_F.

$4d_{xz}/d_{yz}$. Stretching across M and K is also a big arc-like hole pocket mainly derived from Mo $4d_{z^2}$ and B $2p$. Additionally, inside the large hole pocket is a small oval-shaped electron pocket, which mainly comes from Mo $4d_{z^2}$ and $4d_{xz}/d_{yz}$. The highest v_F occurs when crossing the first electron pocket along the Γ-M directions. For W_2B_2H, the energy bands are traversing the Fermi level four, one, and five times along the Γ-M, M-K, and K-Γ directions, respectively, forming three Γ-centered electron pockets, with the inner hexagonal one, owning the lowest v_F, originating mainly from W $5d_{z^2}$ while the next owning the maximum v_F mainly contributed by W $5d_{x^2-y^2}/d_{xy}$. The same as Mo_2B_2H, M-centered is a horseshoed hole pocket dominated by W $5d_{xz}/d_{yz}$. In the middle of K-Γ is also an electron pocket contributed by $5d_{z^2}$ and $5d_{xz}/d_{yz}$. Interestingly, the highest v_F of these four structures always distributes on the Γ-centered pocket. For Al, Mg, Mo based thin films, it is the first pocket, while for W_2B_2H it is the second one.

D. Electron-phonon coupling and possible superconductivity

In order to investigate the EPC strength and superconductivity of these 2D M_2B_2H, the phonon dispersions, phonon density of states (PhDOS), Eliashberg spectral function $\alpha^2F(\omega)$, as well as $\lambda(\omega)$ are calculated and presented in Fig. 4. For comparison, phonon dispersions of M_2B_2 ($M =$ Al, Mg, Mo, W) monolayers are also present in Fig. S2 of the SM [59], which are very consistent with previous work [33]. Phonon dispersions without imaginary modes clearly indicate that these 2D metal diborides are all dynamically stable. The phonon spectrum shows a wide range of frequency extending up to over 1000 cm^{-1}. It is understandable that light elements would generate high phonon frequencies [43,65]. From the decomposition of phonon spectrums with respect to M ($M =$ Al, Mg, Mo, W), B and H atomic vibrations, and the PhDOS, it can be found that for these M_2B_2H monolayers, vibrations of metal atoms dominate the low frequencies, while the intermediate and high frequencies are characterized by vibrations of B and H atoms. Additionally, one out-of-plane mode and two in-plane modes of metal atoms mainly constitute the three acoustic branches for all these M_2B_2H monolayers, and the highest optical branch is always contributed by the vibrations of H atoms.

Specifically, for Al_2B_2H, one may note the apparent Kohn anomaly in the middle along the K-Γ direction in the low-energy region (0–210 cm^{-1}), mainly associated with the in-plane vibrations of Al atoms, contributing 58% of the total EPC ($\lambda = 2.93$). Such kind of Kohn anomaly in the acoustic branch is generally a clue for the softening of the lattice. Phonon dispersion weighted by the magnitude of EPC $\lambda_{\mathbf{q}\nu}$ shown in Fig. 4(b) indicates that the region with the Kohn anomaly in the middle of the K-Γ path possesses the largest EPC, consistent with the integrated EPC distributions presented in Fig. 5(a), which is the sum of the $\lambda_{\mathbf{q}\nu}$ of all phonon branches in the plane of $q_z = 0$ [40]. The phonons (210–610 cm^{-1}) along the Γ-M direction near Γ, mainly associated with the H_{xy} vibrations, corresponding to the Γ-centered red circle area exhibited in Fig. 5(a), contribute 39% of the total EPC. The rest is contributed by the phonons distributed in the high-frequency region associated with the B_{xy} and H_z vibrations, accounting for only about 3%. Three main vibration modes of the Al_2B_2H monolayer at the large EPC magnitude $\lambda_{\mathbf{q}\nu}$ in the BZ are shown in Fig. 6(a), with the vibration frequencies shown below each graph. The arrows represent the directions of atomic vibrations. Since the total EPC constant λ (2.93) of Al_2B_2H is greater than 1.30, belonging to strong-coupling superconductors, the full Allen-Dynes formula is more appropriate for evaluating the superconducting transition temperature T_c. By solving Eqs. (7)–(10), the obtained strong-coupling correction factor and the shape correction factor are $f_1 = 1.218$ and $f_2 = 1.203$, respectively, and finally the obtained T_c for Al_2B_2H is 52.64 K (with $\omega_{\log} = 202.02$ K), exceeding the McMillan limit (39 K). Such value of T_c is smaller than that of the hydrogenated monolayer MgB_2 ($\lambda = 1.46$, $T_c = 67$ K) [43], but higher than β_{12} and χ_3 borophene ($T_c = 18.7$ K and 24.7 K) [25].

For Mg_2B_2H, from Fig. 4(e), frequencies below 320 cm^{-1} are mainly dominated by the vibrations of Mg atoms, while the medium and high frequencies are completely occupied by B and H vibrations. Combined with the phonon dispersion weighted by the magnitude of EPC $\lambda_{\mathbf{q}\nu}$ and PhDOS shown in Figs. 4(f) and 4(g), it can be found that the vibrations below 300 cm^{-1} mainly associated with the Mg_z contribute 48% of the total EPC ($\lambda = 0.86$). Phonons from 340 to 420 cm^{-1}, dominated by B_z vibrations, contribute 16% of the total EPC. The vibrations (420–650 cm^{-1}) in the full BZ, mainly associated with the B_{xy} and H_{xy} vibrations, account for about 32% of the total EPC. The rest is contributed by the phonons distributed in the high-frequency region associated with the H vibrations, accounting for only about 4%. The area with strong EPC is mainly located around the Γ point, consistent with the integrated EPC distributions, with a red hexagonal-like Γ-centered area representing strong EPC, presented in

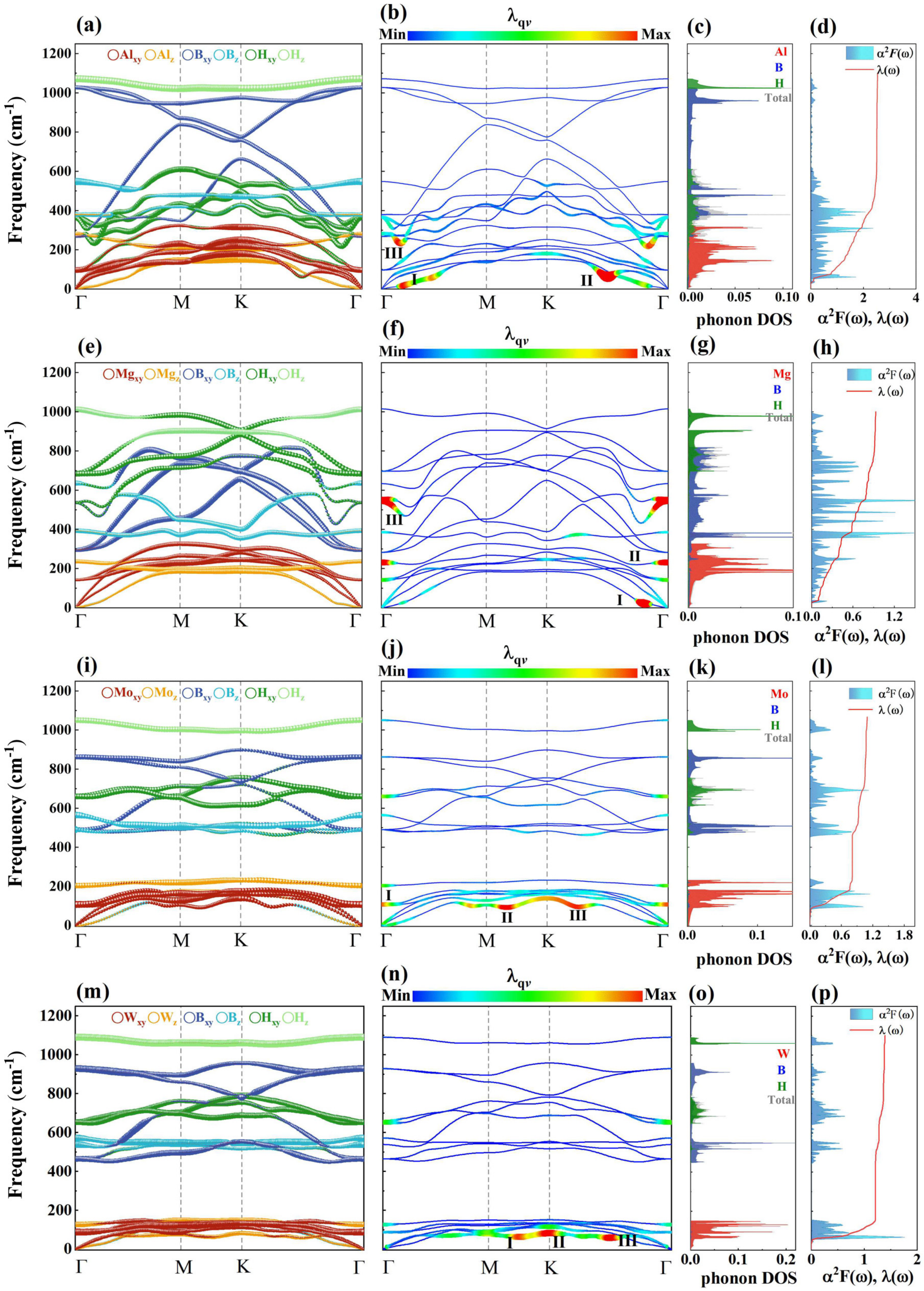

FIG. 4. (a), (e), (i), (m): Phonon dispersions of M_2B_2H weighted by the vibrational modes of M (M = Al, Mg, Mo, W), B, and H atoms. The vibration directions represented by the different colored circles are also shown in the legend. *xy* represent in-plane vibrations and *z* represents out-of-plane vibrations. (b), (f), (j), (n): Phonon dispersion weighted by the magnitude of EPC $\lambda_{\mathbf{q}\nu}$. (c), (g), (k), (o): Total and atom-projected phonon DOS. (d), (h), (l), (p): Eliashberg spectral function $\alpha^2F(\omega)$ and cumulative frequency-dependent EPC function $\lambda(\omega)$.

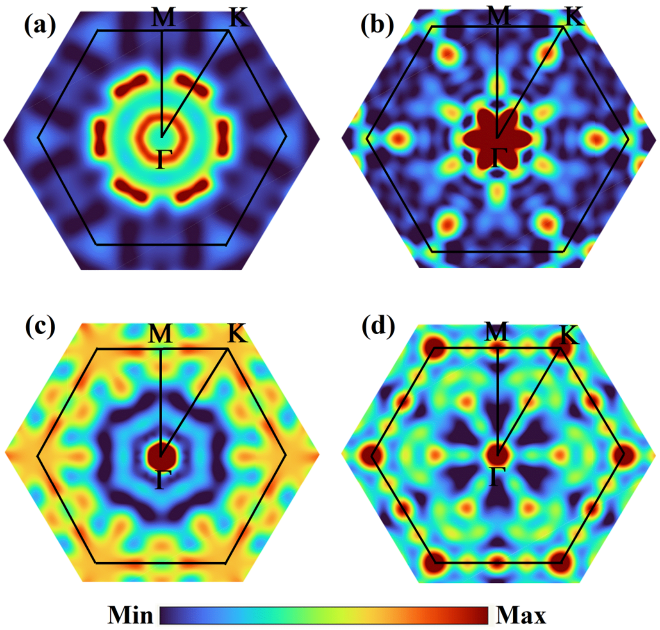

FIG. 5. The integrated EPC distributions of (a) Al_2B_2H, (b) Mg_2B_2H, (c) Mo_2B_2H, and (d) W_2B_2H in the plane of $q_z = 0$. The high-symmetry path of Γ-*M*-*K*-Γ is also marked.

Fig. 5(b). Three main vibration modes at the large EPC magnitude $\lambda_{\mathbf{q}\nu}$ in the BZ are shown in Fig. 6(b) (see also Table III), consistent with the decomposed phonon spectrum presented in Fig. 4(e). The finally obtained EPC value λ for Mg_2B_2H is 0.86 with $T_c = 23.25\,\mathrm{K}$ and $\omega_{\log} = 430.29\,\mathrm{K}$, slightly higher than monolayer MgB_2 ($\lambda = 0.68$, $T_c = 20\,\mathrm{K}$) [42], indicating Mg_2B_2H belongs to intermediate-coupling conventional superconductors.

The phonon spectra of Mo_2B_2H and W_2B_2H are more hierarchical than that of the former two. The reason for this may be the large discrepancy of the atomic mass between metal and nonmetal atoms. The optic phonon bands are more flat and many optic-optic phonon gaps appear. Additionally, different degrees of phonon softening also can be observed within their acoustic-mode range. More specifically, for Mo_2B_2H, the vibration modes can be divided into three parts: Part I is the low-frequency range (0–240 cm^{-1}), where one may note two apparent Kohn anomalies at the lowest acoustic branch in the middle along *M*-*K* and along *K*-Γ near the *K* point. Both of these Kohn anomalies are mainly originated from the in-plane vibrations of Mo atoms. As indicated by Fig. 4(j), two Kohn anomalies made major contributions to the EPC, accounting for approximately 75% of the total EPC ($\lambda = 1.09$). Part II is the intermediate-frequency range (460–590 cm^{-1}) mainly associated with the B_z and H_{xy} vibrations, accounting for about 10% of the total EPC. Part III is the high-frequency region (above 600 cm^{-1}) associated with the B_{xy} and H_z vibrations, accounting for about 15%. As shown in Fig. 5(c), except Γ, the strong-coupling region is mainly distributed at the boundary of the BZ, consistent with Fig. 4(j). The three main vibration modes at the large EPC magnitude $\lambda_{\mathbf{q}\nu}$ in the BZ are shown in Fig. 6(c), consistent with the decomposed phonon spectrum presented in Fig. 4(i). The finally obtained EPC value for Mo_2B_2H is 1.09, with the corresponding $T_c = 21.54\,\mathrm{K}$ and $\omega_{\log} = 277.25\,\mathrm{K}$, smaller than that of Janus MoSH monolayer ($\lambda = 1.40$, $T_c = 28.92\,\mathrm{K}$) [40] but larger than heavily *n*-doped graphene ($\lambda = 0.42$, $T_c = 13\,\mathrm{K}$) [66],

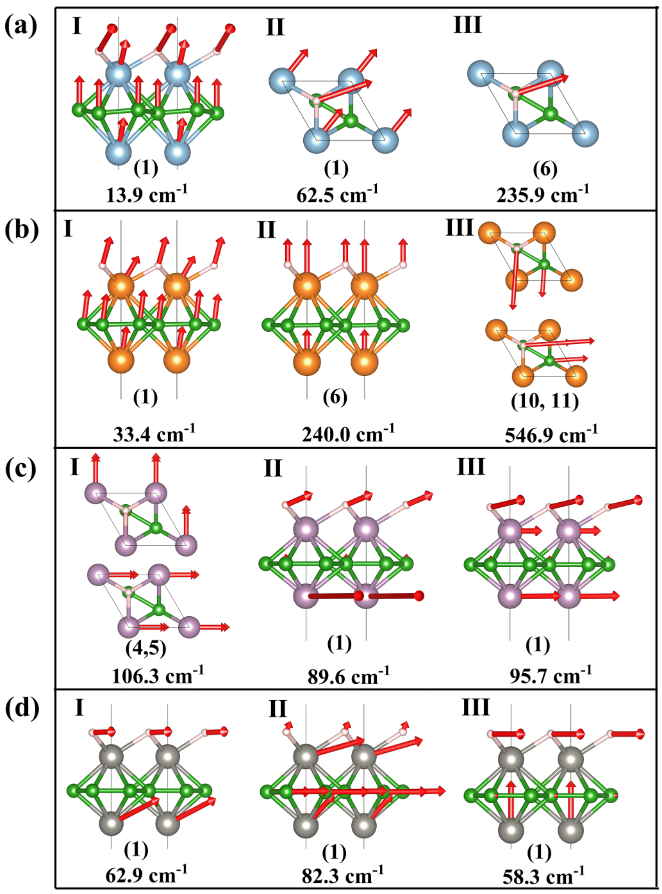

FIG. 6. Vibration modes of (a) Al_2B_2H, (b) Mg_2B_2H, (c) Mo_2B_2H, and (d) W_2B_2H at the marked I, II, and III positions in Fig. 4, which exhibit large EPC and contribute most to the EPC. The arrows represent the directions of the atomic vibrations. The numbers of each mode and the vibration frequencies are also shown below each graph.

TABLE III. The vibration, symmetry, and activity of the modes in Fig. 6. The activity I refers to the inferred modes and R refers to the Raman modes.

	Modes	Vibration	Symmetry	Activity
Al_2B_2H	I	Al_z, B_z, H_z	A'	
	II	Al_{xy}, H_{xy}	A	
	III	H_{xy}	A'	
Mg_2B_2H	I	Mg_z, B_z, H_z	A	
	II	Mg_z, H_z	A_1	I+R
	III	B_{xy}, H_{xy}	E	I+R
Mo_2B_2H	I	Mo_{xy}	E	I+R
	II	Mo_{xy}, H_z	A	
	III	Mo_{xy}, H_{xy}	A	
W_2B_2H	I	W_z, H_{xy}	A	
	II	W_z, B_{xy}, H_z	A	
	III	W_z, H_{xy}	A	

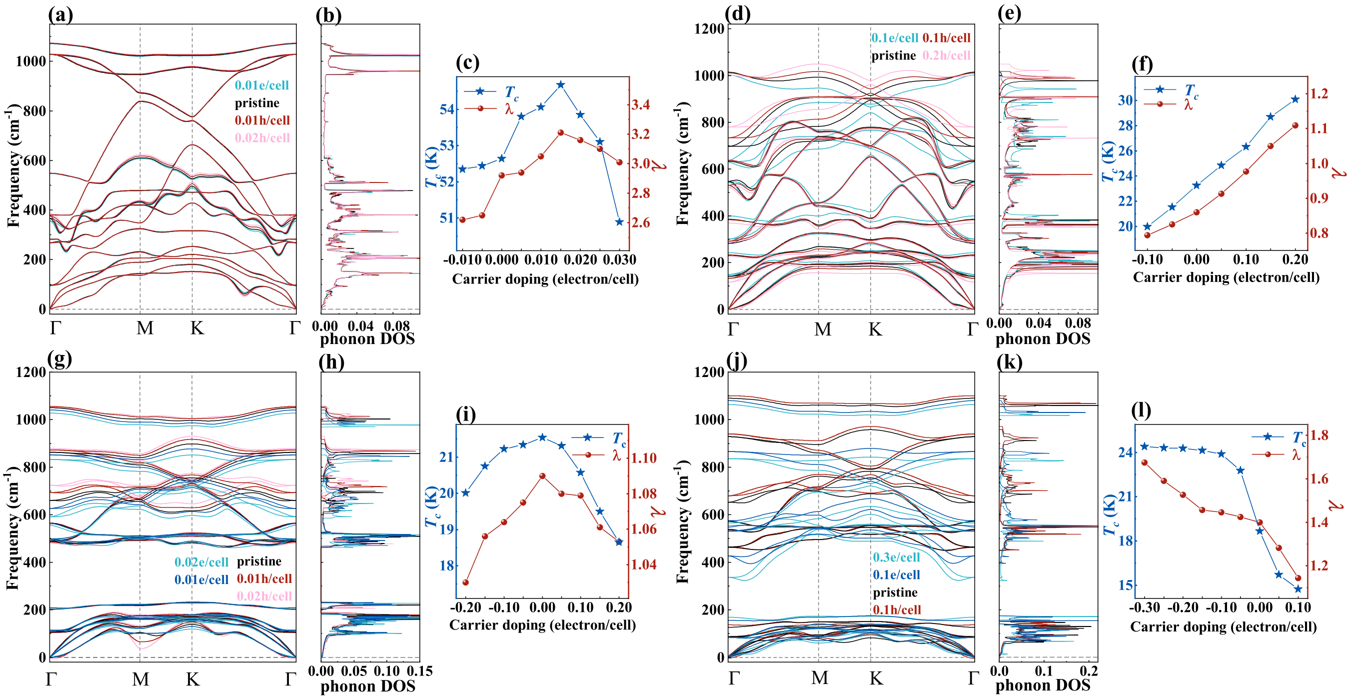

FIG. 7. Phonon dispersions and phonon DOS under different carrier doping for (a), (b) Al_2B_2H; (d), (e) Mg_2B_2H; (g), (h) Mo_2B_2H; and (j), (k) W_2B_2H. Variations of λ (red) and T_c (blue) along with different carrier doping are presented on the right of each phonon spectrum.

indicating that Mo_2B_2H, the same as Mg_2B_2H, belongs to intermediate-coupling conventional superconductors.

Similarly, for W_2B_2H, the areas with strong coupling are also mainly concentrated in the low-energy region. The lowest acoustic branch also has a small softening in the middle of M-K, originating from the vibration modes of W atoms, contribute almost 87% of the total EPC ($\lambda = 1.40$). The intermediate-frequency range (430–630 cm^{-1}) is mainly associated with B vibrations, accounting for 5% of the total EPC. The rest is contributed by the phonons distributed in the high-frequency region associated with B_{xy} and H vibrations, accounting for about 8% of the total EPC. The region with strong EPC is mainly distributed at high symmetry points and between their paths in the low-frequency range, as shown in Fig. 5(d). Three main vibration modes at the large EPC magnitude $\lambda_{\mathbf{q}\nu}$ in the BZ are shown in Fig. 6(d), consistent with the decomposed phonon spectrum presented in Fig. 4(m). Since the total EPC constant λ (1.40) of W_2B_2H is greater than 1.30, the full Allen-Dynes formula is more appropriate for evaluating its T_c. The obtained strong-coupling correction factor and the shape correction factor are $f_1 = 1.081$ and $f_2 = 1.053$, respectively, and the finally obtained T_c and $\omega_{\log}$ are 18.67 K and 153.84 K, respectively, similar to the electron-doped W_2N_3 ($\lambda = 1.43$, $T_c = 22.76$ K) [67].

E. Doping effect

The performance of carrier doping in regulating 2D materials is very impressive [14,15,36,38,40]. For M_2B_2H monolayers, whether it is feasible to enhance superconductivity by carrier doping is worth studying. In this work we adopt a jellium model to simulate the carrier doping effect by directly increasing or reducing the total electron number of the system. For each doping concentration, we fully relax the structure and repeat the calculations of the EPC and superconductivity. The corresponding phonon dispersions and variations of the EPC constant λ and T_c are presented in Fig. 7.

On the premise of ensuring structural dynamical stability, Al_2B_2H can withstand relatively low doping concentration. In Fig. 7(a), the robust phonon dispersion curves indicate a dynamically stable nature. It can be seen that under the action of hole doping, the low-frequency phonon modes tend to be softened, leading to a larger EPC, while in the case of electron doping, the situation is exactly opposite. Results indicate that the EPC strength and T_c of Al_2B_2H under doping exhibit trends of first increasing and then decreasing behaviors. Similarly to tetr-W_2B_2 [68], the largest values of $T_c = 54.67$ K and $\lambda = 3.21$ appear at the hole doping of 0.015 h per cell.

For Mg_2B_2H, there is an almost linear relationship between T_c and λ with carrier doping concentration, as shown in Fig. 7(d). We find that when doping more than 0.2 holes, the phonon spectra will exhibit imaginary frequencies around the Γ point. Thus, the largest value of $T_c = 30.09$ K with $\lambda = 1.11$ appears at the hole doping of 0.2 h per cell.

For Mo_2B_2H, it can be seen that electron doping reduces the phonon modes in the middle and high frequency regions but has little effect on low-energy modes. Interestingly, under hole doping, in the acoustic-mode range of below 100 cm^{-1}, relative to the pristine structure, a more apparent Kohn anomaly appears around the M point, which mainly originates from the in-plane vibrations of Mo atoms and can be enlarged by deep hole doping. However, different from our expectation, the normally phonon softening induced enhancements of EPC and T_c do not occur. Both EPC and T_c are weakened by electron or hole doping, as indicated in Fig. 7(f).

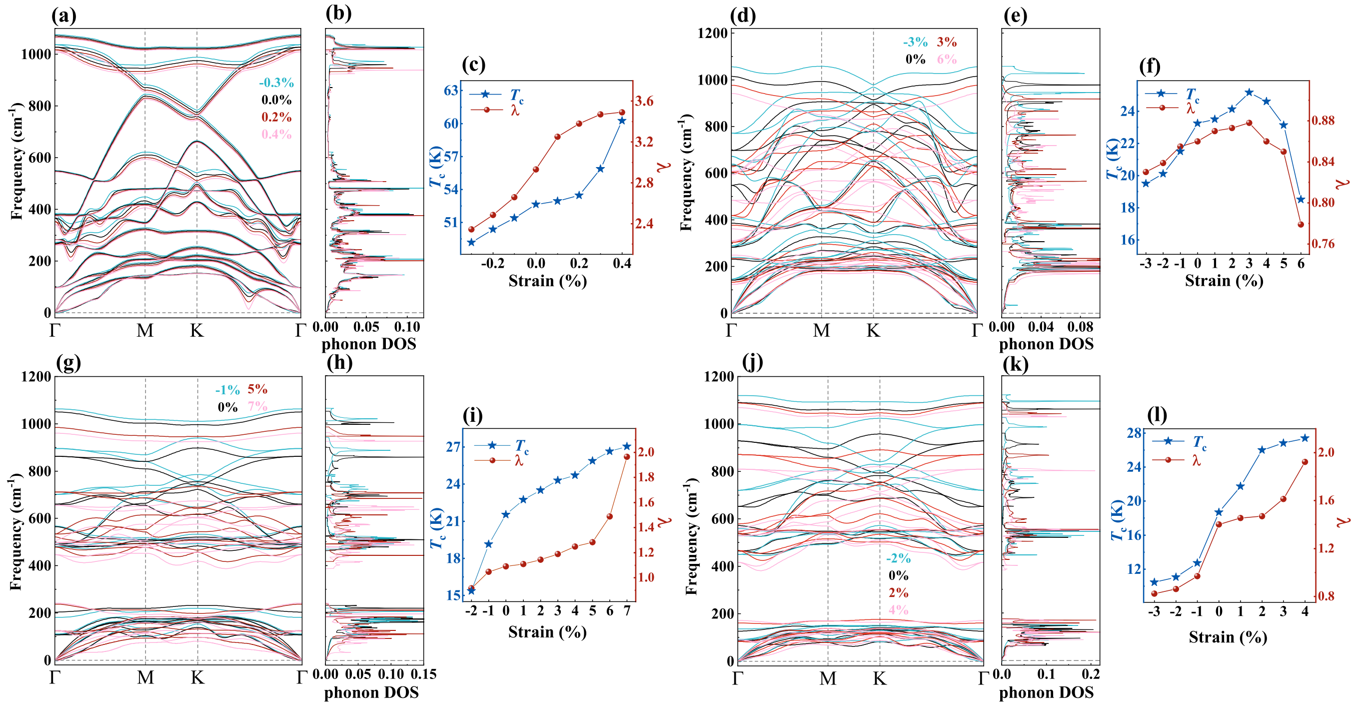

FIG. 8. Phonon dispersions and phonon DOS under different biaxial strains for (a), (b) Al_2B_2H; (d), (e) Mg_2B_2H; (g), (h) Mo_2B_2H; and (j), (k) W_2B_2H. Variations of λ (red) and T_c (blue) along with different strains are presented on the right of each phonon spectrum.

For W_2B_2H, differently from the former cases, the coupling strength and T_c are enhanced by electron doping, since the Fermi level is shifted upward and the $N(E_F)$ is increased. When doping is over 0.1 e/cell, the T_c is no longer changed. After EPC beyond 1.30 under electron doping, the full Allen-Dynes formula is more appropriate for calculating the T_c, and finally the largest value of $T_c = 24.39$ K with $\lambda = 1.68$ for W_2B_2H appears at the electron doping of 0.3 *e* per cell.

Thus, except for Mo_2B_2H, the λ and T_c of the other three systems all exhibit varying degrees of enhancement under the carrier doping effect. This is likely due to the increasing participation of the electrons in the superconducting Cooper pairing. The phonon softening also plays partial role in such enhancement. Anyway, similarly to many other 2D systems [30,69], carrier doping can also regulate the superconductivity of M_2B_2H monolayers.

F. Strain engineering

Since strains will be introduced when the 2D materials are synthesized on appropriate substrates, the superconducting properties should be affected. So the real situation in experiments should be different from our calculated freestanding samples. Therefore, we systematically study the phonon of the strained M_2B_2H monolayers by biaxial strains to simulate the real samples grown on substrates with different lattice constants. The equibiaxial tensile and compressive strains have been applied on these four configurations, calculated by $\varepsilon = \frac{a-a_0}{a_0} \times 100\%$, where a and a_0 are the strained and unstrained lattice constants. The positive value means tensile strain while negative one means compressive strain. For each case, we fully relax the structures and calculate the EPC and superconductivity. The calculated phonon dispersions as well as the variations of the EPC constant λ and T_c are presented in Fig. 8.

We find that the phonon dispersion of Al_2B_2H is very sensitive to the strain, which is only dynamically stable under the strain region of $-1\% \leqslant \varepsilon \leqslant 0.4\%$. For simple comparison, the phonon dispersions under $\varepsilon = -0.3\%$, 0, 0.2%, and 0.4% are displayed in Fig. 8(a). The tensile strain makes the overall phonon frequency downward, while the situation is opposite when compressive strain is applied. The tensile strain causes λ to show a trend of increasing, as shown in Fig. 8(b), while compressive strain always shows negative effects on coupling. Under tensile strain of 0.4%, the largest T_c of about 60.24 K is obtained.

For Mg_2B_2H, it is dynamically stable under the strain region of $-4\% \leqslant \varepsilon \leqslant 9\%$, indicating that it can bear more strain than Al_2B_2H. The effect of strain on phonons is basically similar to that of the Al_2B_2H. The variation in EPC strength presents a trend of first increasing and then decreasing. Under tensile strain of $\varepsilon = 3\%$, the T_c can be modulated up to about 25.17 K, with $\lambda = 0.88$. Compared to the pristine structure ($T_c = 23.25$ K, $\lambda = 0.86$), although tensile strain changes the electronic structure and phonon dispersion to some extent, it induces limited effect on T_c.

The strain range that Mo_2B_2H can withstand is slightly lower than that of the Mg_2B_2H. Phonon spectra under different strains are presented in Fig. 8(e). Unlike hole doping, which causes the Kohn anomaly at the M point, a greater Kohn anomaly will occur under 8% tensile strain in the middle of Γ-M, making it dynamic unstable (see Fig. S6 in the SM [59]). Such kind of unstable phonon mode may also correlate with a possible charge density wave state [70]. When the applied tensile strain is beyond 5%, the EPC strength exceeds 1.30. So the full Allen-Dynes formula is adopted to calculate T_c. The

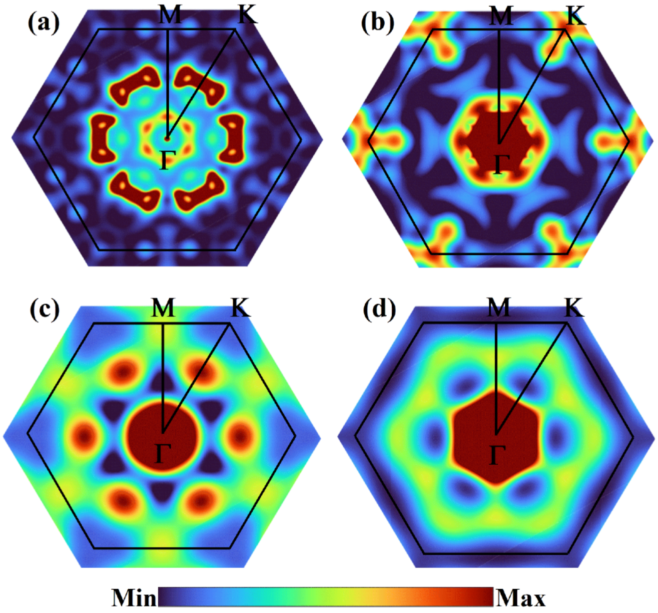

FIG. 9. The integrated EPC distributions of (a) 0.4% tensile strained Al_2B_2H, (b) 0.2 hole-doped Mg_2B_2H, (c) 7% tensile strained Mo_2B_2H, and (d) 4% tensile strained W_2B_2H in the plane of $q_z = 0$.

values of λ and T_c monotonically increase when strain changes from −2% to 7%. The maximum value of $T_c = 27.05$ K with $\lambda = 1.96$ appears when 7% tensile strain is applied.

For W_2B_2H, the low-energy modes do not undergo significant changes under the action of strain, while the variation trend of phonon dispersions in the middle and high frequencies is consistent with the previous three cases. The strength of EPC and T_c also continuously increase under the action of tensile strain. Interestingly, like Mo_2B_2H, W_2B_2H also exhibits an evident Kohn anomaly at the same location under 5% tensile strain along the Γ-*M* path, making it dynamically unstable (see Fig. S6 of the SM [59]). Under maximum tensile strain of $\varepsilon = 4\%$, the finally obtained T_c can be modulated up to about 27.37 K with $\lambda = 1.92$.

Obviously, for M_2B_2H monolayers, tensile strain can always have varying degrees of benefit on the enhancement of EPC and the increase of T_c, which may be due to the softened lower acoustic-phonon branches. Examples of superconductivity being enhanced by tensile strain can also be found in previous works, such as aluminum-deposited graphene [14] and hydrogenated monolayer MgB_2 [43]. Contrarily, phonon hardening induced by compressive strain is confirmed to be always detrimental to the superconducting properties of the structure we studied, differently from type-I ort-CaB_6, hex-CaB_6 [30], $Ti_2B_2H_4$ [44], and tetr-W_2B_2 [68], which undergo a significant enhancement of superconductivity by compressive strain.

G. Discussion

In order to investigate the overall variation of the coupling strength more intuitively, the integrated EPC distributions of four systems in the plane of $q_z = 0$ when they reach the maximum T_c under carrier doping or strain engineering are presented in Fig. 9. Except for Mg_2B_2H, which achieved the most significant enhancement of coupling during hole doping, the maximum increase in λ and T_c of the other three systems occurs when tensile strain is applied. From Fig. 9(a), it can be seen that due to the tensile strain applied to Al_2B_2H being tiny ($\varepsilon = 0.4\%$), the influence on its lattice is relatively limited. So the integrated EPC distribution has not undergone too much change but is more extensive and significant compared to that of the pristine one. The coupling enhancement in the middle region of the *K*-Γ path is the result of phonon softening induced by tensile strain. Since the effect of carrier doping on the lattice is relatively limited compared to that of the strain engineering, for Mg_2B_2H, combined with Figs. 5(b) and 9(b), the original strong-coupling region becomes stronger under doping of 0.2 h/cell, especially around the Γ and *K* points. For Mo_2B_2H and W_2B_2H, tensile strain suppresses the strong coupling at *K* to disappear but induces concentrated and strongly distributed of EPC around Γ. Overall, each structure exhibits some kinds of enhancement of EPC.

For M_2B_2H monolayers, the softened phonon modes tend to result in strong EPC, similarly to 2D borophenes [71], Janus MoSH [40], and W_2N_3 [67], in which the softened modes in the low-energy acoustic phonons are characterized by very large coupling $\lambda_{\mathbf{q}\nu}$. Additionally, as for the main source of EPC, middle and low frequency phonon branches dominate the EPC of Al_2B_2H and Mg_2B_2H, while for Mo_2B_2H and W_2B_2H it is mainly contributed by the lowest acoustic phonon branch associated with metal atoms. This is different when comparing with the hydrogenated monolayer MgB_2 [43], H_3S [72–74], and LaH_{10} [75,76], in which the optical phonon vibrations from H in the intermediate and high frequencies contribute the most to λ, but more similar to monolayer Janus MoSH [40] and W_2N_3 [67].

Typically, it should be noted that the predicted value of T_c is highly sensitive to the choice of the empirical parameter μ^*, as shown in Eq. (5). To explore the sensitivity of T_c with the choice of μ^*, the relationship between them is studied in detail by setting μ^* in the range of 0.05–0.15. For all the M_2B_2H materials, the T_c is decreased monotonically with the increase of μ^*. Take Al_2B_2H for an example; the T_c reaches the largest (63.14 K) when the μ^* is 0.05. As μ^* increases from 0.05 to 0.15, T_c decreases from 63.14 to 44.89 K. In this work, we choose a typical value of $\mu^* = 0.10$ and relevant detailed results are shown in Fig. S7 [59].

In Table IV, we list the superconducting parameters of μ^*, $N(E_F)$, $\omega_{\log}$, EPC constant λ, and T_c for the four M_2B_2H monolayers and other 2D borophenes and boride superconductors. It can be seen that from M_2B_2 (M = Al, Mg, Mo, W) to M_2B_2H, the introduction of the H atom always makes $N(E_F)$ increase, with more obvious enhancement of λ and T_c. Especially for Al_2B_2, hydrogenation makes its T_c increase from almost 0 to over 50 K. For M_2B_2H (M = Al, Mg, Mo, W), $N(E_F)$ always increases after doping or strain engineering, while T_c and λ are also enlarged, indicating that the $N(E_F)$ has a positive effect on superconductivity.

The comparison of T_c before and after hydrogenation of the four systems, as well as the maximum T_c they can achieve under the application of external regulation, is shown in Fig. 10. Here, one can intuitively see that hydrogenation has a significant benefit on increasing the T_c of M_2B_2. Additionally, for Al_2B_2H and Mg_2B_2H, the superconductivity is dominated by the *s* orbital of metal atoms and B-p_z, while for Mo_2B_2H

TABLE IV. Superconducting parameters of μ^*, $N(E_F)$ (states/spin/Ry/unit cell), logarithmically averaged phonon frequency $\omega_{\log}$ (K), EPC constant λ, and superconducting T_c (K) for 2D M_2B_2H and several other 2D metal boride superconductors.

Materials	Doping	ε	μ^*	$N(E_F)$	$\omega_{\log}$	λ	T_c	Refs.
χ_3			0.10		323.43	0.95	24.70	[25]
β_{12}			0.10		384.16	0.89	18.70	[25]
BL-B_8			0.10	7.98	495.51	0.61	11.9	[29]
BL-B_{30}			0.10	27.01	541.05	0.47	4.9	[29]
B_2O			0.10	5.30	255.00	0.75	10.35	[77]
MgB_2			0.13			0.68	20.00	[42]
AlB_2			0.13			1.13	26.50	[31]
NbB_2			0.13		245.00	2.23	35.50	[33]
CaB_2			0.13		360.00	1.67	41.60	[33]
CaB_3H			0.10		371.50	1.39	39.30	[41]
MgB_2H			0.13			1.46	67.00	[43]
$Ti_2B_2H_4$			0.10	19.78	550.60	1.18	48.60	[44]
Al_2B_2			0.10	3.71	244.74	0.29	0.10	this work
Mg_2B_2			0.10	9.78	493.19	0.43	3.26	this work
Mo_2B_2			0.10	16.59	291.15	0.40	1.12	this work
W_2B_2			0.10	11.47	231.43	0.38	0.31	this work
Al_2B_2H			0.10	8.34	202.02	2.93	52.64	this work
	0.015 h/cell		0.10	8.58	194.80	3.21	54.67	this work
		0.4%	0.10	8.85	188.41	3.49	60.24	this work
Mg_2B_2H			0.10	10.24	430.29	0.86	23.25	this work
	0.2 h/cell		0.10	11.33	372.35	1.11	30.09	this work
		3%	0.10	10.49	444.66	0.88	25.17	this work
Mo_2B_2H			0.10	25.03	277.25	1.09	21.54	this work
		7%	0.10	26.53	153.38	1.96	27.05	this work
W_2B_2H			0.10	19.33	153.84	1.40	18.67	this work
	0.3 e/cell		0.10	20.86	145.79	1.68	24.39	this work
		4%	0.10	19.56	158.97	1.92	27.37	this work

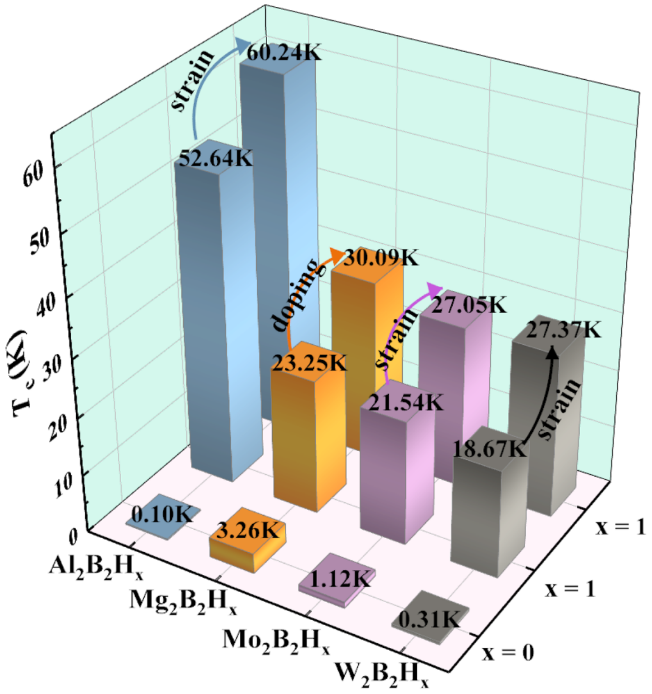

FIG. 10. T_c comparison of 2D M_2B_2, hydrogenated M_2B_2, i.e., M_2B_2H, and doping or straining regulated M_2B_2H (M = Al, Mg, Mo, W).

and W_2B_2H it is their 4*d* and 5*d* orbital electrons playing the critical role, respectively. In hydrogenated monolayer MgB_2 [43], the π-H*s* state formed by hybridizing B-p_z and H-*s* orbitals contributes the most to superconductivity, while for pure boron systems [25,29], CaB_3H [41], and B_2O [77], it is the electrons from B that dominant. This is different from the four systems investigated in our present work, as metal atoms always play a crucial role in the electronic structure and superconducting properties, especially for Mo_2B_2H and W_2B_2H. These behaviors are more similar to $Ti_2B_2H_4$ [44] and Janus MoSH [40], in which superconductivity is mainly dominated by the electrons from metal atoms. Therefore, the M_2B_2H monolayers we investigated provide a new platform for exploring the origin of superconductivity in different electron orbitals and prove once again the significant role of external control conditions of hydrogenation, carrier doping, and strain engineering.

H. Anisotropic effect in monolayer M_2B_2H, taking Al_2B_2H for example

Considering that the electron-phonon Wannier (EPW) code [78–81] can better describe the superconducting energy gap and the electron-phonon coupling (EPC) of layered or low-dimensional systems with respect to the traditional McMillan approximation [82], we, therefore, take Al_2B_2H for example, applying the fully anisotropic Migdal-Eliashberg

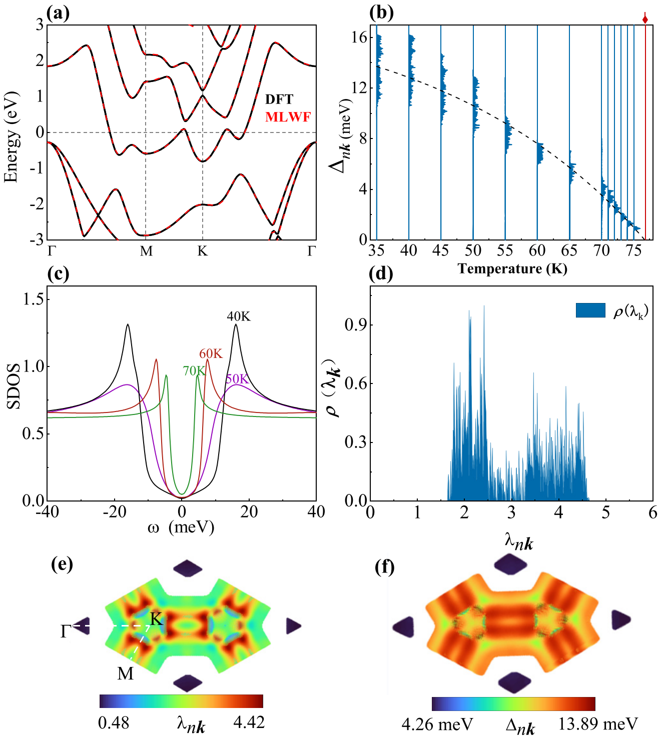

FIG. 11. Anisotropic effect in monolayer Al_2B_2H. (a) Comparison of band structures obtained by density functional theory (DFT) (black lines) and interpolation with MLWF (red dashed lines). (b) Energy distribution of the anisotropic superconducting gap as a function of temperature. (c) Corresponding quasiparticle density of states (DOS) for four representative temperatures. Quasiparticle DOS in the superconducting state, relative to the DOS in the normal state $N_s(\omega)/N_N(\omega)$, as a function of frequency. The SDOS is scaled to coincide with normal DOS, which can facilitate comparing with experimental detection. (d) Distribution of the anisotropic EPC strength λ_k. The momentum-resolved EPC (e) λ_{nk} and superconducting gaps (f) Δ_{nk} on the Fermi surface at $T = 5$ K.

equations to investigate the EPC parameter λ_{nk} and superconducting energy gap Δ_{nk}. Maximally localized Wannier function (MLWF) [83] calculations are performed in a uniform unshifted BZ k-point grid of $12 \times 12 \times 1$, and the s and p orbitals of Al, p_z orbitals of B atoms, including ten Wannier functions, are used to construct MLWF in Al_2B_2H, as shown in Fig. 11(a). A fine k-point grid of $240 \times 240 \times 1$ and q-point grid of $120 \times 120 \times 1$ are adopted to interpolate the anisotropic Migdal-Eliashberg equations, which is sufficient to ensure the convergence. The fermion Matsubara frequency cutoff is set to 0.7 eV; a reasonable setting is 4 times higher than the largest phonon frequency, and here is almost 5.

Shown in Fig. 11(c) is the superconducting density of states (SDOS) under four representative temperatures; the results show a single superconducting energy gap since the SDOS has only one peak, consistent with energy distribution of the anisotropic superconducting gap shown in Fig. 11(b). This is reasonable since Al_2B_2H has only a single band crossing the Fermi level, and does not exhibit significantly different orbital components around it, so that it does not lead to the formation of multiple energy gaps. This feature is distinct from the multigap MgB4 [32], MoSH [40], MgB_2 [42,84,85], and LiBC [86] monolayers, where the σ and π orbitals lead to separate superconducting gaps, but more similar to MgB_2H [43] and t-/h-CuH_2 [87], which exhibit only one single gap. The largest λ_{nk} of Al_2B_2H is associated with Al 3s and 3p states along the M-K direction with a low Fermi velocity, as shown in Fig. 11(e). The resulting λ_{nk}, up to 4.42, is about 1.5 times as large as the isotropic one, and the finally obtained EPC strength ∼2.95, similar to the isotropic $\lambda \sim 2.93$. At $T = 5$ K, presented in Fig. 11(f), the Δ_{nk} is located along the M-K direction on the Fermi surface with a maximum value of 13.89 meV, showing distributions similar to that of the EPC. The superconducting energy gap vanishes at ∼76 K, which is identified as the critical temperature T_c. The T_c obtained by solving anisotropic Migdal-Eliashberg equations is about 44% larger than that of the isotropic results (∼52.6 K).

IV. CONCLUSION

In this work, based on first-principles calculations, we predict a series of 2D hydrogenated metal borides M_2B_2H (M = Al, Mg, Mo, W), and investigate their crystal structure, bonding properties, electronic structures, phonon dispersions, dynamic stability, EPC strength, superconducting properties, and so on. Based on the Eliashberg theory, by analytically solving the McMillan-Allen-Dynes formula, we find that these four 2D materials are all intrinsic phonon-mediated superconductors with the T_c of 52.64, 23.25, 21.54, and 18.67 K, respectively. Among them, there are two strong-coupling superconductors with large EPC constants λ of 2.93 for Al_2B_2H and 1.40 for W_2B_2H, while two intermediate-coupling conventional superconductors of Mg_2B_2H and Mo_2B_2H with EPC constants λ of 0.86 and 1.09, respectively. The EPC of Al_2B_2H and Mg_2B_2H is mainly governed by the vibrations of metal and B atoms, while for Mo_2B_2H and W_2B_2H is almost controlled by the metal atoms. Additionally, we also explore the effects of electron/hole doping and tensile/compressive strains on the superconducting properties. The results of doping indicate that hole doping obviously enhances the EPC and increases the T_c of Al_2B_2H and Mg_2B_2H, while for W_2B_2H the enhancement of EPC and T_c occurs during electron doping. For Mo_2B_2H, doping is always detrimental for its superconductivity. Under the action of biaxial tensile strain, both EPC and T_c of these four systems can be increased, while compressive strain always weakens the coupling. Combining results of doping and strain engineering, except for Mg_2B_2H, which achieves the most significant enhancement of coupling during hole doping, the maximum increase in λ and T_c of the other three systems occurs when tensile strain is applied. A large T_c of 60.24 K for Al_2B_2H is obtained under applying 0.4% biaxial tensile strain, while the T_c of the other three systems also exceeds 25 K under proper doping or strain. These M_2B_2H monolayers provide another option for experiments beyond the 2D boron to realize superconductivity in boron-based 2D materials. Our research provides new guidance for the study of 2D superconductors and enriches the database of 2D metal borides, which are beneficial to further theoretical and experimental studies of electronic structures and superconductivity in other 2D metal diborides.

ACKNOWLEDGMENTS

This work is supported by the National Natural Science Foundation of China (Grants No. 12074213, No. 11574108, and No. 12074381), the Natural Science Foundation of Shandong Province (Grants No. ZR2021ZD01 and No. ZR2023MA082), and the Project of Introduction and Cultivation for Young Innovative Talents in Colleges and Universities of Shandong Province. The calculations were performed at CSNS Scientific Computing Platform of Institute of High Energy Physics of CAS and GBA Sub-center of National HEP Science Data Center.

[1] K. S. Novoselov, A. K. Geim, S. V. Morozov, D. Jiang, Y. Zhang, S. V. Dubonos, I. V. Grigorieva, and A. A. Firsov, Science **306**, 666 (2004).

[2] B. Aufray, A. Kara, S. Vizzini, H. Oughaddou, C. Léandri, B. Ealet, and G. Le Lay, Appl. Phys. Lett. **96**, 183102 (2010).

[3] P. Vogt, P. De Padova, C. Quaresima, J. Avila, E. Frantzeskakis, M. C. Asensio, A. Resta, B. Ealet, and G. Le Lay, Phys. Rev. Lett. **108**, 155501 (2012).

[4] A. Splendiani, L. Sun, Y. Zhang, T. Li, J. Kim, C.-Y. Chim, G. Galli, and F. Wang, Nano Lett. **10**, 1271 (2010).

[5] B. Radisavljevic, A. Radenovic, J. Brivio, V. Giacometti, and A. Kis, Nat. Nanotechnol. **6**, 147 (2011)

[6] Q. H. Wang, K. Kalantar-Zadeh, A. Kis, J. N. Coleman, and M. S. Strano, Nat. Nanotechnol. **7**, 699 (2012).

[7] A. K. Geim and I. V. Grigorieva, Nature (London) **499**, 419 (2013).

[8] K. Watanabe, T. Taniguchi, and H. Kanda, Nat. Mater. **3**, 404 (2004).

[9] K. S. Novoselov, D. Jiang, F. Schedin, T. Booth, V. Khotkevich, S. Morozov, and A. K. Geim, Proc. Natl. Acad. Sci. USA **102**, 10451 (2005).

[10] Y. Guo, Y.-F. Zhang, X.-Y. Bao, T.-Z. Han, Z. Tang, L.-X. Zhang, W.-G. Zhu, E. G. Wang, Q. Niu, Z. Q. Qiu, J.-F. Jia, Z.-X. Zhao, and Q.-K. Xue, Science **306**, 1915 (2004).

[11] T. Uchihashi, Supercond. Sci. Technol. **30**, 013002 (2017).

[12] G. Profeta, M. Calandra, and F. Mauri, Nat. Phys. **8**, 131 (2012).

[13] B. M. Ludbrook, G. Levy, P. Nigge. M. Zonno, M. Schneider, D. J. Dvorak. C. N. Veenstra, S. Zhdanovich, D. Wong, P. Dosanjh, C. Straßer, A. Stöhr, S. Forti, C. R. Ast, U. Starke, and A. Damascelli, Proc. Natl. Acad. Sci. USA **112**, 11795 (2015).

[14] H.-Y. Lu, Y. Yang, L. Hao, W. S. Wang, L. Geng, M. Zheng, Y. Li, N. Jiao, P. Zhang, and C. S. Ting, Phys. Rev. B **101**, 214514 (2020).

[15] G. Savini, A. C. Ferrari, and F. Giustino, Phys. Rev. Lett. **105**, 037002 (2010).

[16] W. Wan, Y. Ge, F. Yang, and Y. Yao, Europhys. Lett. **104**, 36001 (2013).

[17] D. F. Shao, W. J. Lu, H. Y. Lv, and Y. P. Sun, Europhys. Lett. **108**, 67004 (2014).

[18] Y. Ge, W. Wan, F. Yang, and Y. Yao, New J. Phys. **17**, 035008 (2015).

[19] N. W. Ashcroft, Phys. Rev. Lett. **21**, 1748 (1968).

[20] S. Azadi, B. Monserrat, W. M. C. Foulkes, and R. J. Needs, Phys. Rev. Lett. **112**, 165501 (2014).

[21] R. P. Dias and I. F. Silvera, Science **355**, 715 (2017).

[22] Y. X. Liu, Y. J. Dong, Z. Y. Tang, X. F. Wang, L. Wang, T. J. Hou, H. P. Lin, and Y. Y. Li, J. Mater. Chem. C **4**, 6380 (2016).

[23] E. S. Penev, A. Kutana, and B. I. Yakobson, Nano Lett. **16**, 2522 (2016).

[24] Y. C. Zhao, S. M. Zeng, and J. Ni, Appl. Phys. Lett. **108**, 242601 (2016).

[25] M. Gao, Q.-Z. Li, X.-W. Yan, and J. Wang, Phys. Rev. B **95**, 024505 (2017).

[26] H. Tang and S. Ismail-Beigi, Phys. Rev. Lett. **99**, 115501 (2007).

[27] A. J. Mannix, X. F. Zhou, B. Kiraly, J. D. Wood, D. Alducin, B. D. Myers, X. Liu, B. L. Fisher, U. Santiago, J. R. Guest, M. J. Yacaman, A. Ponce, A. R. Oganov, M. C. Hersam, and N. P. Guisinger, Science **350**, 1513 (2015).

[28] B. Feng, J. Zhang, Q. Zhong, W. Li, S. Li, H. Li, P. Cheng, S. Meng, L. Chen, and K. Wu, Nat. Chem. **8**, 563 (2016).

[29] L. Yan, R. Ku, J. Zou, L. Zhou, J. Zhao, X. Jiang, and B.-T. Wang, RSC Adv. **11**, 40220 (2021).

[30] T. Bo, P. F. Liu, L. Yan, and B. T. Wang, Phys. Rev. Mater. **4**, 114802 (2020).

[31] Y. C. Zhao, C. Lian, S. M. Zeng, Z. H. Dai, S. Meng, and J. Ni, Phys. Rev. B **100**, 094516 (2019).

[32] Y. C. Zhao, C. Lian, S. M. Zeng, Z. H. Dai, S. Meng, and J. Ni, Phys. Rev. B **101**, 104507 (2020).

[33] C. Sevik, J. Bekaert, M. Petrov, and M. V. Milošević, Phys. Rev. Mater. **6**, 024803 (2022).

[34] Z. Wang, S. Zeng, Y. Zhao, X. Wang, and J. Ni, Phys. Rev. B **104**, 174519 (2021).

[35] L. Liu, X. Liu, P. Song, L. Zhang, X. Huang, W. Zhang, Z. Zhang, and Y. Jia, Nano Lett. **23**, 1924 (2023).

[36] J. O. Sofo, A. S. Chaudhari, and G. D. Barber, Phys. Rev. B **75**, 153401 (2007).

[37] Y.-P. Li, L. Yang, H.-D. Liu, N. Jiao, M.-Y. Ni, N. Hao, H.-Y. Lu, and P. Zhang, Phys. Chem. Chem. Phys. **24**, 9256 (2022).

[38] T. B. Rawal, L. H. Chang, H. D. Liu, H. Y. Lu, and C. S. Ting, Phys. Rev. Mater. **6**, 054003 (2022).

[39] A.-Y. Lu, H. Zhu, J. Xiao, C.-P. Chuu, Y. Han, M.-H. Chiu, C.-C. Cheng, C.-W. Yang, K.-H. Wei, Y. Yang, Y. Wang, D. Sokaras, D. Nordlund, P. Yang, D. A. Muller, M.-Y. Chou, X. Zhang, and L.-J. Li, Nat. Nanotechnol. **12**, 744 (2017).

[40] P.-F. Liu, F. Zheng, J. Li, J.-G. Si, L. Wei, J. Zhang, and B.-T. Wang, Phys. Rev. B **105**, 245420 (2022).

[41] L. Yang, Y.-P. Li, H.-D. Liu, N. Jiao, M.-Y. Ni, H.-Y. Lu, P. Zhang, and C. S. Ting, Chin. Phys. Lett. **40**, 017402 (2023).

[42] J. Bekaert, A. Aperis, B. Partoens, P. M. Oppeneer, and M. V. Milošević, Phys. Rev. B **96**, 094510 (2017).

[43] J. Bekaert, M. Petrov, A. Aperis, P. M. Oppeneer, and M. V. Milošević, Phys. Rev. Lett. **123**, 077001 (2019).

[44] Y.-L. Han, Y.-P. Li, L. Yang, H.-D. Liu, N. Jiao, B.-T. Wang, H.-Y. Lu, and P. Zhang, Mater. Today Phys. **30**, 100954 (2023).

[45] W. Kohn, A. D. Becke, and R. G. Parr, J. Phys. Chem. **100**, 12974 (1996).

[46] P. Giannozzi, S. Baroni, N. Bonini, M. Calandra, R. Car, C. Cavazzoni, D. Ceresoli, G. L. Chiarotti, M. Cococcioni, I. Dabo *et al.*, J. Phys.: Condens. Matter **21**, 395502 (2009).

[47] P. Giannozzi, O. Baseggio, P. Bonfà, D. Brunato, R. Car, I. Carnimeo, C. Cavazzoni, S. de Gironcoli, P. Delugas, F. F. Ruffino, A. Ferretti, N. Marzari, I. Timrov, A. Urru, and S. Baroni, J. Chem. Phys. **152**, 154105 (2020).

[48] M. Schlipf and F. Gygi, Comput. Phys. Commun. **196**, 36 (2015).

[49] D. R. Hamann, Phys. Rev. B **88**, 085117 (2013).

[50] P. E. Blöchl, Phys. Rev. B **50**, 17953 (1994).

[51] S. Baroni, S. De Gironcoli, A. Dal Corso, and P. Giannozzi, Rev. Mod. Phys. **73**, 515 (2001).

[52] G. Kresse and J. Furthmüller, Phys. Rev. B **54**, 11169 (1996).

[53] W. L. McMillan, Phys. Rev. **167**, 331 (1968).

[54] R. C. Dynes, Solid State Commun. **10**, 615 (1972).

[55] P. B. Allen and R. C. Dynes, Phys. Rev. B **12**, 905 (1975).

[56] G. Henkelman, A. Arnaldsson, and H. Jónsson, Comput. Mater. Sci. **36**, 354 (2006).

[57] A. Savin, R. Nesper, S. Wengert, and T. F. Fässler, Angew. Chem. Int. Ed. Engl. **36**, 1808 (1997).

[58] B.-T. Wang, P. Souvatzis, O. Eriksson, and P. Zhang, J. Chem. Phys. **142**, 174702 (2015).

[59] See Supplemental Material at http://link.aps.org/supplemental/10.1103/PhysRevMaterials.7.114802 for (I) lattice structure, (II) phonon dispersions, electronic structures, $\alpha^2F(\omega)$, and EPC constant λ of M_2B_2 (M = Al, Mg, Mo, W) monolayers, (III) different configurations for hydrogenation of monolayer M_2B_2, (IV) electron localization function, (V) AIMD simulations, (VI) phonon dispersions beyond the limit of biaxial tensile strain, and (VII) evaluated T_c as a function of Coulomb pseudopotential μ^* of M_2B_2H (M = Al, Mg, Mo, W) monolayers.

[60] Y.-J. Chen, H.-Y. Lu, F.-L. Shao, and P. Zhang, Phys. Rev. Mater. **7**, 034004 (2023).

[61] B.-T. Wang, W. Zhang, and W.-D. Li, Sci. Adv. Mater. **5**, 1916 (2013).

[62] Y. Wang, F. Li, Y. Li, and Z. Chen, Nat. Commun. **7**, 11488 (2016).

[63] L. M. Yang, V. Bacic, I. A. Popov, A. I. Boldyrev, T. Heine, T. Frauenheim, and E. Ganz, J. Am. Chem. Soc. **137**, 2757 (2015).

[64] B. Feng, B. Fu, S. Kasamatsu, S. Ito, P. Cheng, C.-C. Liu, Y. Feng, S. Wu, S. K. Mahatha, P. Sheverdyaeva, P. Moras, M. Arita, O. Sugino, T.-C. Chiang, K. Shimada, K. Miyamoto, T. Okuda, K. Wu, L. Chen, Y. Yao *et al.*, Nat. Commun. **8**, 1007 (2017).

[65] D. Duan, Y. Liu, Y. Ma, Z. Shao, B. Liu, and T. Cui, Natl. Sci. Rev. **4**, 121 (2017).

[66] E. R. Margine and F. Giustino, Phys. Rev. B **90**, 014518 (2014).

[67] J. Chen and Y. Ge, Phys. Rev. B **103**, 064510 (2021).

[68] L. Yan, T. Bo, W. Zhang, P.-F. Liu, Z. Lu, Y.-G. Xiao, M.-H. Tang, and B.-T. Wang, Phys. Chem. Chem. Phys. **21**, 15327 (2019).

[69] B.-T. Wang, P.-F. Liu, T. Bo, W. Yin, O. Eriksson, J. Zhao, and F. Wang, Phys. Chem. Chem. Phys. **20**, 12362 (2018).

[70] B.-T. Wang, P.-F. Liu, J.-J. Zheng, W. Yin, and F. Wang, Phys. Rev. B **98**, 014514 (2018).

[71] Y. Zhao, S. Zeng, C. Lian, Z. Dai, S. Meng, and J. Ni, Phys. Rev. B **98**, 134514 (2018).

[72] A. P. Drozdov, M. I. Eremets, I. A. Troyan, V. Ksenofontov, and S. I. Shylin, Nature (London) **525**, 73 (2015).

[73] D. Duan, Y. Liu, F. Tian, D. Li, X. Huang, Z. Zhao, H. Yu, B. Liu, W. Tian, and T. Cui, Sci. Rep. **4**, 6968 (2015).

[74] Y. Li, J. Hao, H. Liu, Y. Li, and Y. Ma, J. Chem. Phys. **140**, 174712 (2014).

[75] A. P. Drozdov, P. P. Kong, V. S. Minkov, S. P. Besedin, M. A. Kuzovnikov, S. Mozaffari, L. Balicas, F. F. Balakirev, D. E. Graf, V. B. Prakapenka, E. Greenberg, D. A. Knyazev, M. Tkacz, and M. I. Eremets, Nature (London) **569**, 528 (2019).

[76] M. Somayazulu, M. Ahart, A. K. Mishra, Z. M. Geballe, M. Baldini, Y. Meng, V. V. Struzhkin, and R. J. Hemley, Phys. Rev. Lett. **122**, 027001 (2019).

[77] L. Yan, P.-F. Liu, H. Li, Y. Tang, J. He, X. Huang, B.-T. Wang, and L. Zhou, npj Comput. Mater. **6**, 94 (2020).

[78] F. Giustino, M. L. Cohen, and S. G. Louie, Phys. Rev. B **76**, 165108 (2007).

[79] J. Noffsinger, F. Giustino, B. D. Malone, C.-H. Park, S. G. Louie, and M. L. Cohen, Comput. Phys. Commun. **181**, 2140 (2010).

[80] S. Poncé, E. Margine, C. Verdi, and F. Giustino, Comput. Phys. Commun. **209**, 116 (2016).

[81] F. Giustino, Rev. Mod. Phys. **89**, 015003 (2017).

[82] E. R. Margine and F. Giustino, Phys. Rev. B **87**, 024505 (2013).

[83] A. A. Mostofi, J. R. Yates, Y.-S. Lee, I. Souza, D. Vanderbilt, and N. Marzari, Comput. Phys. Commun. **178**, 685 (2008).

[84] H. J. Choi, D. Roundy, H. Sun, M. L. Cohen, and S. G. Louie, Nature (London) **418**, 758 (2002).

[85] Y. An, J. Li, K. Wang, G. Wang, S. Gong, C. Ma, T. Wang, Z. Jiao, X. Dong, G. Xu, R. Wu, and W. Liu, Phys. Rev. B **104**, 134510 (2021).

[86] P. Modak, A. K. Verma, and A. K. Mishra, Phys. Rev. B **104**, 054504 (2021).

[87] X. Yan, S. Ding, X. Zhang, A. Bergara, Y. Liu, Y. Wang, X. F. Zhou, and G. Yang, Phys. Rev. B **106**, 014514 (2022).